

Three-dimensional reconstruction of the ν -AlCrFe phase by electron crystallography

X. D. Zou,^{a*} Z. M. Mo,^{a†} S. Hovmöller,^a X. Z. Li^b and K. H. Kuo^c

^aStructural Chemistry, Stockholm University, SE-106 91 Stockholm, Sweden, ^bCenter for Materials Research and Analysis, 104 N Walter Scott Engineering Center, University of Nebraska-Lincoln, Lincoln, NE 68588-0656, USA, and ^cBeijing Laboratory of Electron Microscopy, Institute of Physics, Chinese Academy of Sciences, PO Box 603, 100080, Beijing, People's Republic of China.
Correspondence e-mail: zou@struc.su.se

The three-dimensional (3D) structure of the huge quasicrystal approximant ν -AlFeCr (space group $P6_3/m$, $a = 40.687$ and $c = 12.546$ Å) was solved by electron crystallography. High-resolution transmission-electron-microscopy (HREM) images and selected-area electron diffraction patterns from 13 different zone axes were combined to give a 3D potential map. 124 out of 129 unique atoms were found in the 3D map. Procedures for *ab initio* structure determination by 3D reconstruction are given. It is demonstrated that 3D reconstruction from HREM images is very powerful for solving structures – even very complicated ones. There is no limit in terms of the number of unique atoms in a structure that can be solved by 3D reconstruction.

© 2003 International Union of Crystallography
Printed in Great Britain – all rights reserved

1. Introduction

Electron crystallography is a powerful method for solving structures of crystals with submicrometre sizes, which are too small for X-ray crystallography. One of the main advantages of electron crystallography over X-ray crystallography is that the phases of crystallographic structure factors can be obtained directly from HREM images, when the crystal is thin enough to nearly satisfy kinematic approximation. A rapidly increasing number of inorganic crystal structures, including minerals, oxides and metal clusters, have been solved by electron crystallography during the last ten years (Weirich, 2001). In most cases, the structures were solved from high-resolution electron-microscopy (HREM) images using Fourier-transform-based crystallographic image processing. Selected-area electron diffraction (SAED) patterns have also been used alone for structure determination, where reflections were phased by direct methods (Weirich *et al.*, 2000) or by the Patterson method (Gjønnes *et al.*, 1998).

Most inorganic structures that have been solved by crystallographic image processing have had one short (<4 Å) unit-cell axis (Hovmöller *et al.*, 1984; Wang *et al.*, 1988; Weirich *et al.*, 1996; Zandbergen *et al.*, 1997), in which case it is possible to solve the three-dimensional (3D) structure from a single projection, since there are no overlapping atoms in the projection down such a short axis. For crystals lacking a short axis, there is generally no single projection in which all atoms are well resolved. In such cases, it is not possible to directly interpret HREM images in terms of atomic structures. One

way to solve such structures is to collect electron diffraction patterns from different zone axes of the crystal to get an essentially complete 3D electron diffraction data set. Direct methods or the Patterson method can then be applied to phase the data, similar to what is done in X-ray diffraction (Gjønnes *et al.*, 1998; Wagner *et al.*, 1999; Gemmi *et al.*, 2000).

As a structure becomes more complex and the number of unique atoms increases, phases derived by direct methods become less reliable, especially when the electron diffraction data deviate from the kinematical approximation because of dynamic effects. HREM combined with crystallographic image processing provides a unique method for determining such structures. HREM images from a number of projections along different zone axes may be combined into a 3D potential map, as demonstrated by Wenk *et al.* (1992) on the mineral staurolite. Wenk *et al.* took HREM images to a resolution of 1.38 Å from five different zone axes using an ultra-high-voltage electron microscope (800 kV). All the 16 unique atomic positions including oxygen were resolved in the 3D map reconstructed from the five projections with 59 unique reflections. However, that work was not an *ab initio* structure determination since the structure model obtained by X-ray diffraction was used for determining the common origin and for scaling the amplitudes from different projections.

In order to develop a general procedure of 3D reconstruction by electron crystallography and to see if there is any limit of structure complexity using this method, we applied the 3D reconstruction technique to a very complex structure – the quasicrystal approximant ν -Al_{80.61}Cr_{10.71}Fe_{8.68}. The crystal is hexagonal (space group $P6_3/m$) with very large lattice parameters, $a = 40.687$ and $c = 12.546$ Å. Recently, single-crystal

† Present address: c/o IVF, Argongatan 30, SE-431 53 Mölndal, Sweden.

X-ray diffraction data were obtained from very small needle-like crystals. Owing to the complexity of the structure, it was not possible to solve it by Patterson or direct methods. Fortunately, ν -Al_{80.61}Cr_{10.71}Fe_{8.68} was found to be related to two other known compounds, κ -Al₇₆Cr₁₈Ni₆ (Sato *et al.*, 1997; Li *et al.*, 1997; Marsh, 1998) and λ -Al₄Mn (Kreiner & Franzen, 1997), so a partial structure model could be deduced from them. A complete structure model was obtained from the Fourier map and finally refined (Mo *et al.*, 2000). There are 131 unique atomic sites and in total about 1184 atoms in the unit cell.

The present investigation was undertaken in order to see if an unknown inorganic structure of this complexity could be solved *ab initio* by 3D electron crystallography, *i.e.* without using any prior knowledge from the structurally related compounds. For this purpose, the structure data from Mo *et al.* (2000) were not used through the whole procedure, except for the comparison of final results.

2. Data collection

Samples for electron-microscopy observation were thin films prepared from ingots with nominal composition Al₁₂Fe₂Cr by

slicing, grinding and ion-beam thinning. In this way, it was possible to obtain crystals with large thin areas.

HREM images and electron diffraction (ED) patterns of the ν -AlCrFe crystals were collected on JEOL 3010 (point resolution 1.7 Å) and JEOL 4000 EX (point resolution 1.6 Å) electron microscopes at 300 and 400 kV, respectively. Since the tilt range of these microscopes is very limited ($\pm 15^\circ$), it is only possible to collect data from one or a few of all the zone axes that are needed for 3D reconstruction from each crystallite. In order to determine which zone axes should be chosen for collecting HREM images, a nearly complete 3D electron diffraction data set was collected (Fig. 1).

Three tilt series of ED patterns, tilted along the $(h00)$, $(00l)$ and $(2h, -h, 0)$ axes, were collected on a JEOL 2000FX electron microscope, which allows a specimen tilt of $\pm 45^\circ$. From these tilt series, 13 zone axes that contained strong and/or many reflections were chosen for 3D reconstruction: $[001]$, $[010]$, $[011]$, $[012]$, $[013]$, $[014]$, $[021]$, $[023]$, $[120]$, $[121]$, $[122]$, $[241]$ and $[5, 18, 0]$. For each of the 13 zone axes, through-focus series with three to five HREM images were recorded on film at 500000 magnification. In order to minimize dynamic effects, only the thinnest edges of the crystals were selected for further processing. The corresponding ED patterns were also

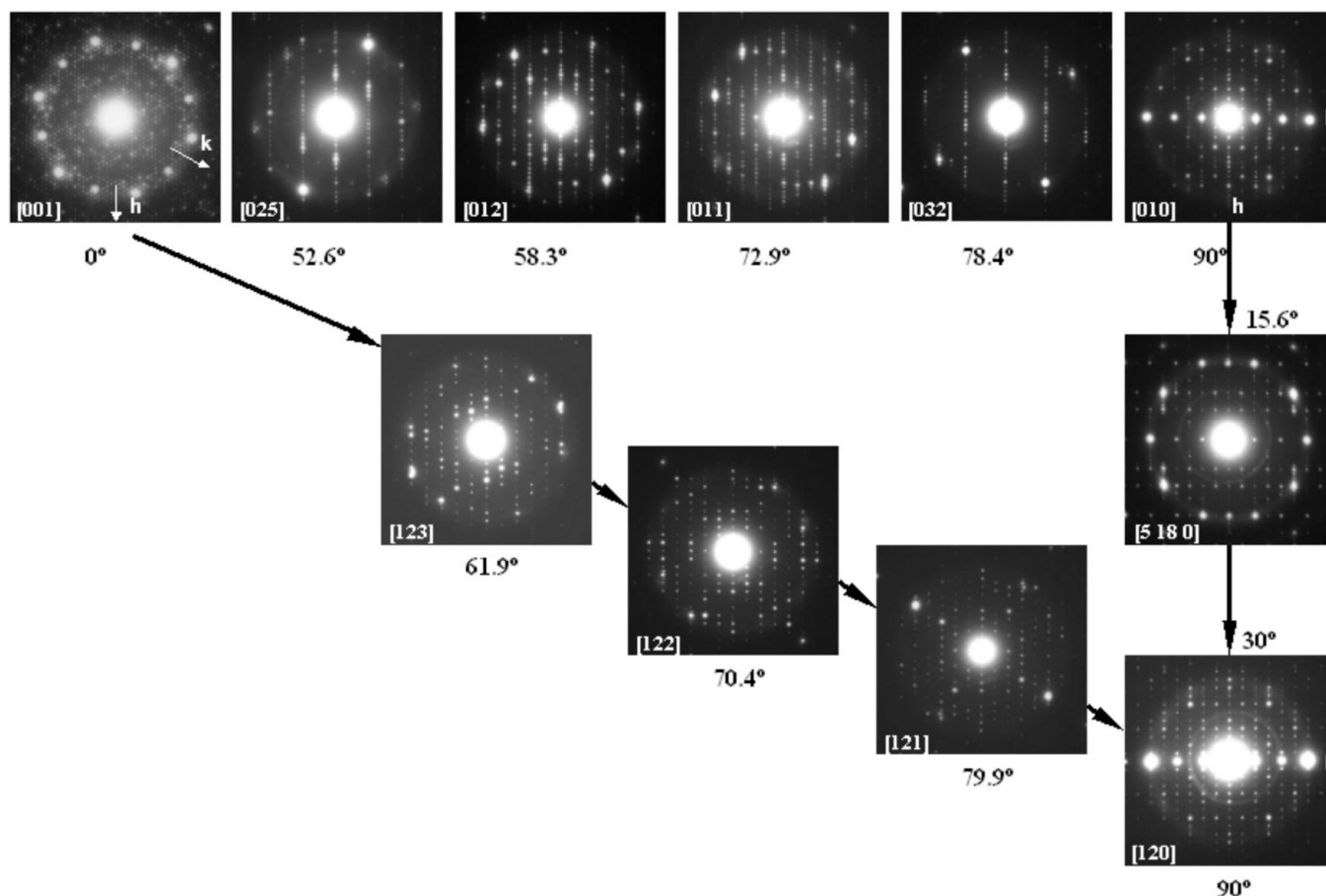


Figure 1

Some of the ED patterns used for sampling the reciprocal space of the ν -AlCrFe phase. The corresponding zone axes and tilt angles from the $[001]$ and $[010]$ zone axes are given.

recorded, as exposure series using 1, 2, 4, 8, 16, 32, 64, 128 and 180 s. The number of ED patterns needed in an exposure series depends on the intensity difference between the strongest and the weakest reflections.

3. Digitization of HREM images and ED patterns

Negatives of HREM images were digitized at 0.6 Å per pixel on a light box by an 8-bit CCD camera (MTI CCD 72) and a SHARK frame grabber using the program *CRISP* (Hovmöller, 1992). Preliminary examinations with Fourier transformations were conducted to assess the general quality, *i.e.* crystallinity, resolution, defocus, astigmatism and so on.

Since the intensity difference between strong and weak spots in an ED pattern is very large, negatives of ED patterns were digitized with a 12-bit slow-scan CCD camera Kite (Calidris, 2000a), which has a dynamic range of more than 2.5 optical density units. The data were first corrected for the response of each of the 1280 by 1024 individual pixels of the

CCD camera and then converted from transmission to optical density values in the following way. For each exposure series, a black image (I_b) with the lens covered by the lens cap was taken in order to measure the dark current of each pixel in the CCD camera. A white image (I_w) with the direct light from the light box was taken to measure response for transmitted light. The dark image was subtracted both from each digitized ED pattern (I_{ED}) and from the white image, using the image calculator function in *CRISP*. Finally, the ED pattern is converted from transmission to optical density units I_{OD} by logarithmation

$$I_{OD}(xy) = \log \frac{I_w(xy) - I_b(xy)}{I_{ED}(xy) - I_b(xy)}.$$

$I_{OD}(xy)$ is scaled to fit to 0–255 grey scale (8 bit).

Intensities of all reflections for each thus corrected negative were extracted by the program *ELD* (Zou *et al.*, 1993). To make sure that the intensities were within the usable range of the CCD camera, intensities of the strongest reflections were

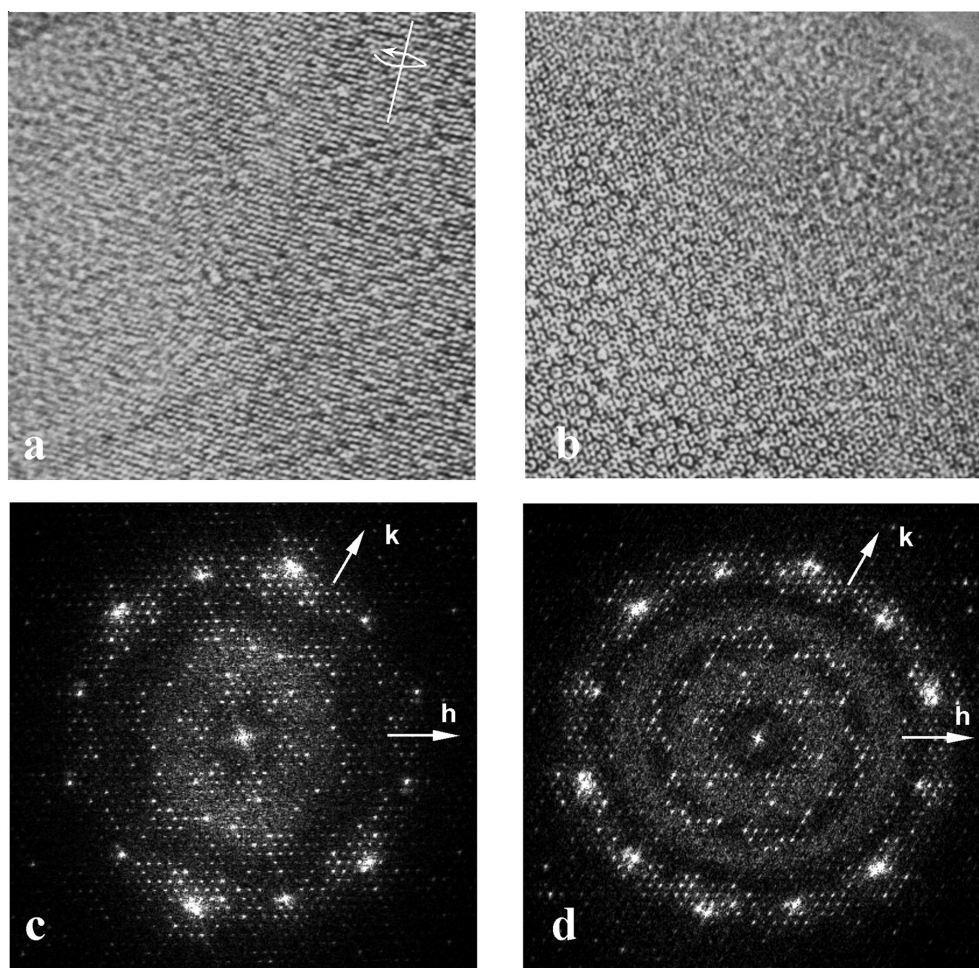


Figure 2 (a), (b) HREM images of the [001] zone axis taken at two different defocus values and their corresponding Fourier transforms [(c) from (a) and (d) from (b)]. The 12 very strong reflections are all at about 2.1 Å resolution. One dark ring in (c) and two dark rings in (d) are seen. These correspond to the zero cross overs of the contrast transfer function (CTF). Both images are astigmatic, since the dark rings are elliptical. The crystal in (a) is more misaligned than that in (b) so the image in (a) is more smeared out in the direction perpendicular to the tilt axis [indicated in (a)].

Table 1

Comparison of structure-factor phases of ν -AlFeCr obtained by electron crystallography (ϕ_{sym}) and X-ray crystallography (ϕ_{xray}).

Image 1 is shown in Fig. 2(a), image 2 in Fig. 2(b). The two images were taken at different defocus values from different crystals. The 50 strongest $hk0$ reflections are listed. 43 of the 45 common reflections have the same phase values from the two HREM images; the other two are marked *. 40 out of the 50 have the same phase as in X-ray crystallography – the differing 10 are marked #.

h	k	l	Amp _{ED}	Image 1			ϕ_{sym}	Image 2			ϕ_{sym}	ϕ_{xray}
				h, k	$k, -h-k$	$h+k, -k$		h, k	$k, -h-k$	$h+k, -k$		
9	0	0	1122	3	-18	-16	0	-7	1	-18	0	180#
14	0	0	1027	-36	177	169	180*	-15	14	-58	0*	0#
8	1	0	1441	-151	176	180	180	165	-170	-175	180	0#
14	1	0	1444	-152	-19	-155	180	-9	-123	-179	180	180
15	1	0	1176	29	42	-16	0	-66	-6	-7	0	0
16	1	0	784	29	21	25	0	-82	27	-14	0	0
13	2	0	2252	-155	-25	-111	180	-26	-106	-175	180	180
14	2	0	1868	-146	-97	-174	180	76	-169	174	180	180
15	2	0	818	-173	-119	-168	180					180
9	3	0	1053	-45	16	-47	0	55	-50	-54	0	180#
14	3	0	1089	20	27	-7	0	-90	19	-13	0	0
1	4	0	812	179	179	162	180	171	-172	-178	180	180
12	4	0	777	44	-137	62	0	-153	69	6	0	0
13	4	0	1237	27	65	-19	0					0
14	4	0	2417	-166	-146	178	180	97	-166	169	180	180
2	5	0	1438	7	-17	-24	0	2	-11	-4	0	0
5	5	0	939	6	-38	-2	0	-6	20	3	0	180#
12	5	0	934	14	31	22	0	-64	20	-5	0	0
13	5	0	1613	-129	-152	142	180	130	-179	173	180	180
14	5	0	7517	27	47	-8	0	-86	15	-15	0	0
10	6	0	2146	-165	177	110	180	-156	155	171	180	180
12	6	0	1228	19	43	4	0	-65	8	4	0	0
14	6	0	1346	9	100	-9	0	-125	5	-9	0	0
3	7	0	1017	19	-33	7	0	10	-23	17	0	180#
5	7	0	995	2	-21	-9	0	6	6	0	0	0
11	7	0	2628	28	22	-6	0	-47	20	-1	0	0
12	7	0	986	36	20	-35	0					0
3	8	0	1597	-175	150	141	180	-171	168	178	180	180
4	8	0	1001	177	150	156	180	-165	-178	177	180	180
9	8	0	2051	36	58	138	0	-134	160	12	0	0
11	8	0	1100	19	10	-30	0	-63	13	-24	0	0
2	9	0	1245	177	136	155	180	-176	165	175	180	180
4	9	0	1042					38	-41	-99	0	180#
8	9	0	978	37	150	127	180	-165	162	16	180	0#
9	9	0	815	17	3	71	0					0
6	10	0	1017	-6	-19	86	0	-13	179	-11	0	180#
7	10	0	1179	-124	-96	-44	0	25	-30	-141	0	180#
10	10	0	1060	1	38	2	0	-70	19	-26	0	0
4	11	0	765	-15	-24	29	0	3	71	-11	0	0
8	11	0	960	28	13	30	0	-57	72	8	0	0
5	13	0	6113	-4	4	46	0	-40	68	-6	0	0
6	13	0	1304	2	29	8	0	-79	50	-19	0	0
7	13	0	998	-174	-152	-129	180	111	-122	-172	180	180
2	14	0	1027	-177	-159	-43	180*	147	13	-136	0*	180#
3	14	0	973	-166	179	-106	180	136	-66	180	180	180
5	14	0	1242	172	-148	-167	180	133	-115	176	180	180
6	14	0	824	-173	-141	-146	180	99	-127	164	180	180
2	15	0	1007	-169	179	-149	180	138	-73	172	180	180
5	15	0	964	-7	32	25	0	-77	63	-19	0	0
1	16	0	875	-17	-4	80	0	-32	124	16	0	0

only extracted from the negatives with the shortest exposure times, while intensities of the weakest reflections were obtained only from those with longer exposure times. Data sets from negatives with different exposure times were merged, using the program *Triple* (Calidris, 2000b). The scale factors were calculated by comparing the intensities of the common reflections (typically over 100 per pair of negatives). All R_{merge} values for pairs of films, differing in exposure time, were less than 8% for all orientations.

4. 2D image processing

Before performing 3D reconstruction, HREM images from each zone axis were studied by crystallographic image processing using *CRISP*. First, a Fourier transform (FT) was calculated for each image and the quality of the image was judged from the resolution, thickness and alignment of the crystal. The defocus and astigmatism values were estimated from the contrast transfer function (CTF) that could be seen

from the FT of the amorphous region of the crystal. Two images of the highest quality for each zone axis were selected for further processing. Here the [001] zone axis is used as an example to demonstrate the steps of 2D image processing to obtain amplitudes and phases of the crystallographic structure factors for each zone axis.

Two HREM images of the [001] zone axis taken at different defocus values; image 1 (Fig. 2*a*) and image 2 (Fig. 2*b*) were used for image processing. For each image, a Fourier transform was calculated from the thinnest part of the crystal (Fig. 2*c* for image 1 and Fig. 2*d* for image 2).

4.1. Determination of the defocus and astigmatism

Since the area selected was from the thinnest part of the crystal, it could be considered as a weak phase object. For a weak phase object, the Fourier transform of the image $I(u)$ is related to the Fourier transform of the projected potential $\Phi(u)$ by

$$I(u) = D(u) \sin \chi(u) \Phi(u),$$

where $D(u) \sin \chi(u)$ is the contrast transfer function (CTF), $D(u)$ is the damping function of the CTF and

$$\chi(u) = \pi \varepsilon u^2 + (\pi C_s \lambda^3 u^4) / 2,$$

where ε is the defocus value, C_s is the spherical aberration constant and λ the wavelength.

The amplitudes of the Fourier transform $I(u)$ are zero where $\sin \chi(u) = 0$, *i.e.* no information at these positions in reciprocal space are transferred to the image. These positions are zero crossover(s) of the CTF. The defocus value(s) can be estimated from the position(s) u of the CTF crossover, and C_s and λ (Zou *et al.*, 1996).

In the Fourier transform of image 1 (Fig. 2*c*), one dark ring is seen at the d value 3.1 Å, marking the zero crossover of the CTF. The position of the dark ring (marked with a red circle in Fig. 3*a*) was very clear when a large amorphous region was included. The defocus value was estimated to be about -700 Å, with an astigmatism of ± 57 Å (Fig. 3*a*). The corresponding CTFs in the two perpendicular directions are shown in Fig. 3*(c)*. The Fourier transform of image 1 (Fig. 2*c*) did not show perfect sixfold symmetry, owing to a slight crystal misalignment. The CTF for image 2 was determined in a similar way from the two dark rings at d values about 4 and 2.5 Å (marked with red circles in Fig. 3*b*). The defocus value was estimated to be -932 Å, with an astigmatism of ± 65 Å.

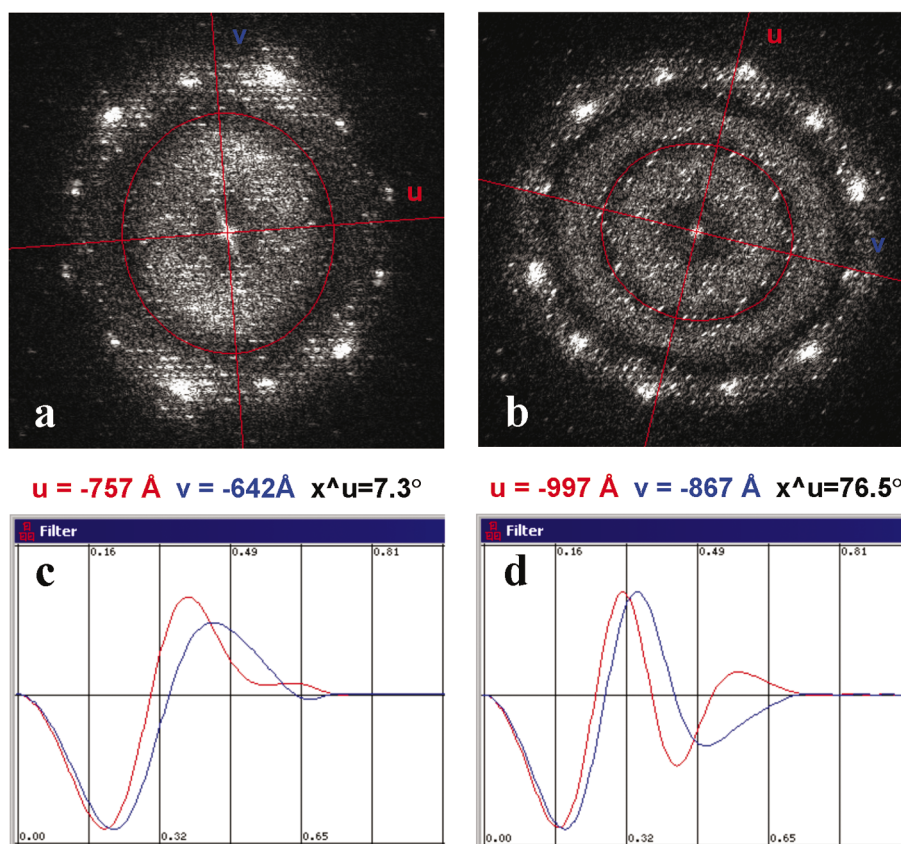


Figure 3

The defocus and astigmatism values in each HREM image were estimated from the dark rings in the Fourier transform using an elliptical approximation by *CRISP*. The left column is from the HREM image in Fig. 2*(a)* and the right column from Fig. 2*(b)*. (*a*), (*b*) The innermost dark ring was fitted by an elliptic ring (marked by red) with the minor and major axes along u and v , respectively. The corresponding defocus values along u and v , as well as the rotating angle of the minor axis u from the horizontal axis x are -757 Å, -642 Å and 7.3°, respectively for (*a*) and -997 Å, -867 Å and 76.5°, respectively for (*b*). (*c*), (*d*) The corresponding CTF curves along the u (in red) and v (in blue) directions for (*a*) and (*b*), respectively. The CTF correction was carried out by shifting the phases of those reflections that lie at the negative CTF by 180°.

4.2. Compensation for the defocus and astigmatism

Once the CTF is determined, the Fourier transform of the projected potential $\Phi(u)$ can be retrieved by

$$\Phi(u) = \frac{I(u)}{D(u)\sin\chi(u)}.$$

This method applies for both crystalline and non-crystalline samples. At those regions in the Fourier transform where the CTF is positive, $\Phi(u)$ and $I(u)$ have the same phases while, at those regions where the CTF is negative, the phases of $\Phi(u)$ are shifted by 180° by the CTF compared with the phase of $I(u)$. We compensated for the effect of the CTF by adding 180° to the phases at those regions where the CTF is negative. Since the amplitudes of $\Phi(u)$ are obtained by dividing the ampli-

tudes of $I(u)$ by the CTF, this correction is very sensitive to the accuracy of the CTF determination and to the extent of the validity of the weak-phase-object approximation, especially when the CTF is close to the zero crossovers. We found that the final results (projected potential maps) often became worse when the amplitudes were also compensated for the effects of the CTF. Thus, we only compensated the phases for the effects of the CTF. The amplitudes for all the reflections were taken from the corresponding electron diffraction patterns, which are not affected by the CTF.

4.3. Lattice refinement and extracting amplitudes and phases

After the phases of the Fourier transform were compensated for the effects of the CTF, the 2D reciprocal

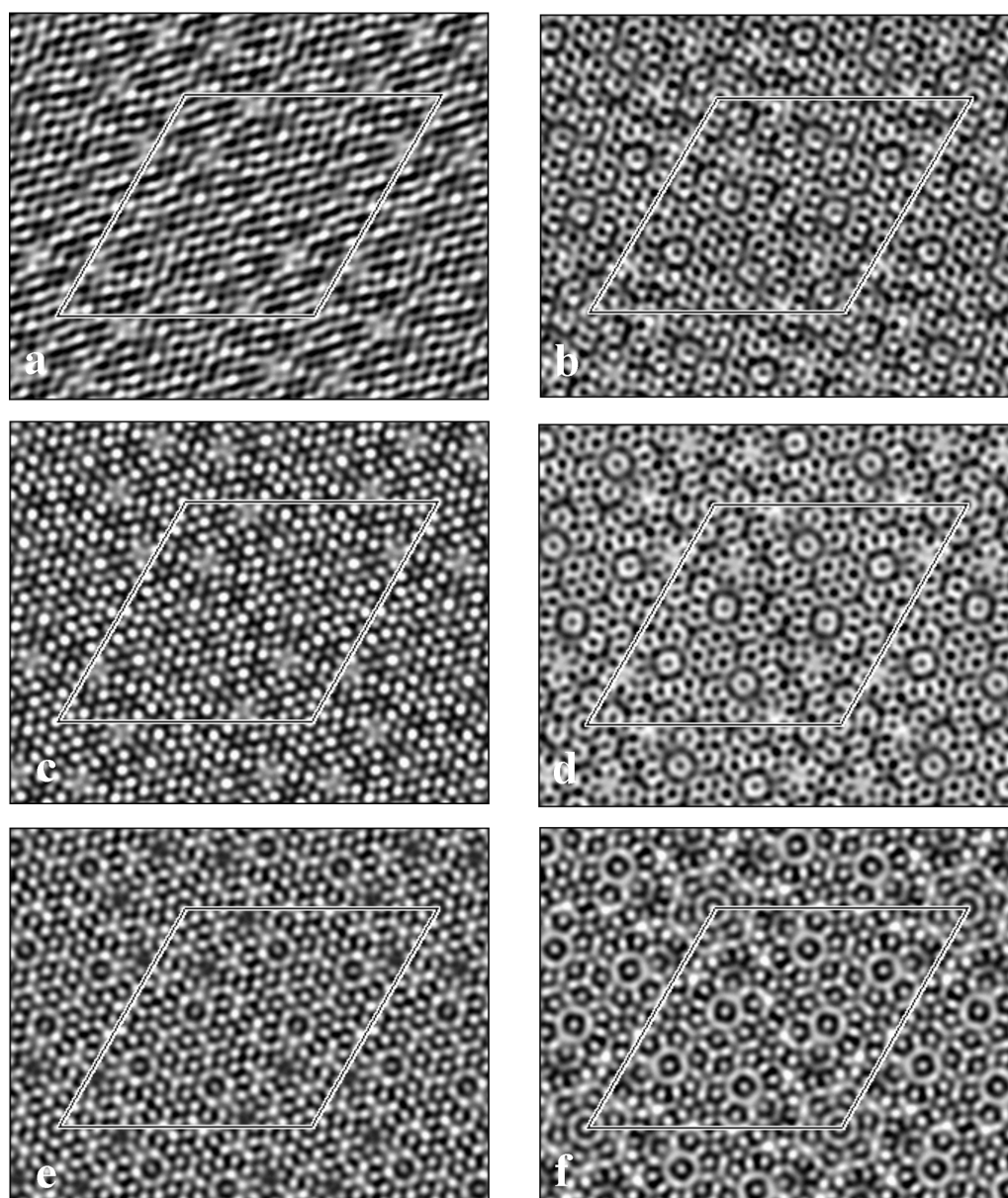


Figure 4

Projected potential maps of the ν phase at various stages of image processing. (a), (b) Only lattice averaging of the original images. (c), (d) After imposing the $p6$ symmetry. (e), (f) After correction of CTF and imposing the $p6$ symmetry. Left column from image 1, right column from image 2.

lattice was determined and refined using all the diffraction spots in the Fourier transform. The amplitude of each reflection was extracted by integrating a 3×3 pixel area around the reflection (with the background subtracted) and the phase was taken from the refined position of the reflection in the Fourier transform, as described by Hovmöller (1992).

4.4. Symmetry determination and origin refinement

The 2D symmetry for each projection can be determined by analysing the phase values. For different symmetries, the phase relations between symmetry-related reflections are different. When the projection is centrosymmetric, the phases are restricted to 0 or 180° . Since phases are not absolute values

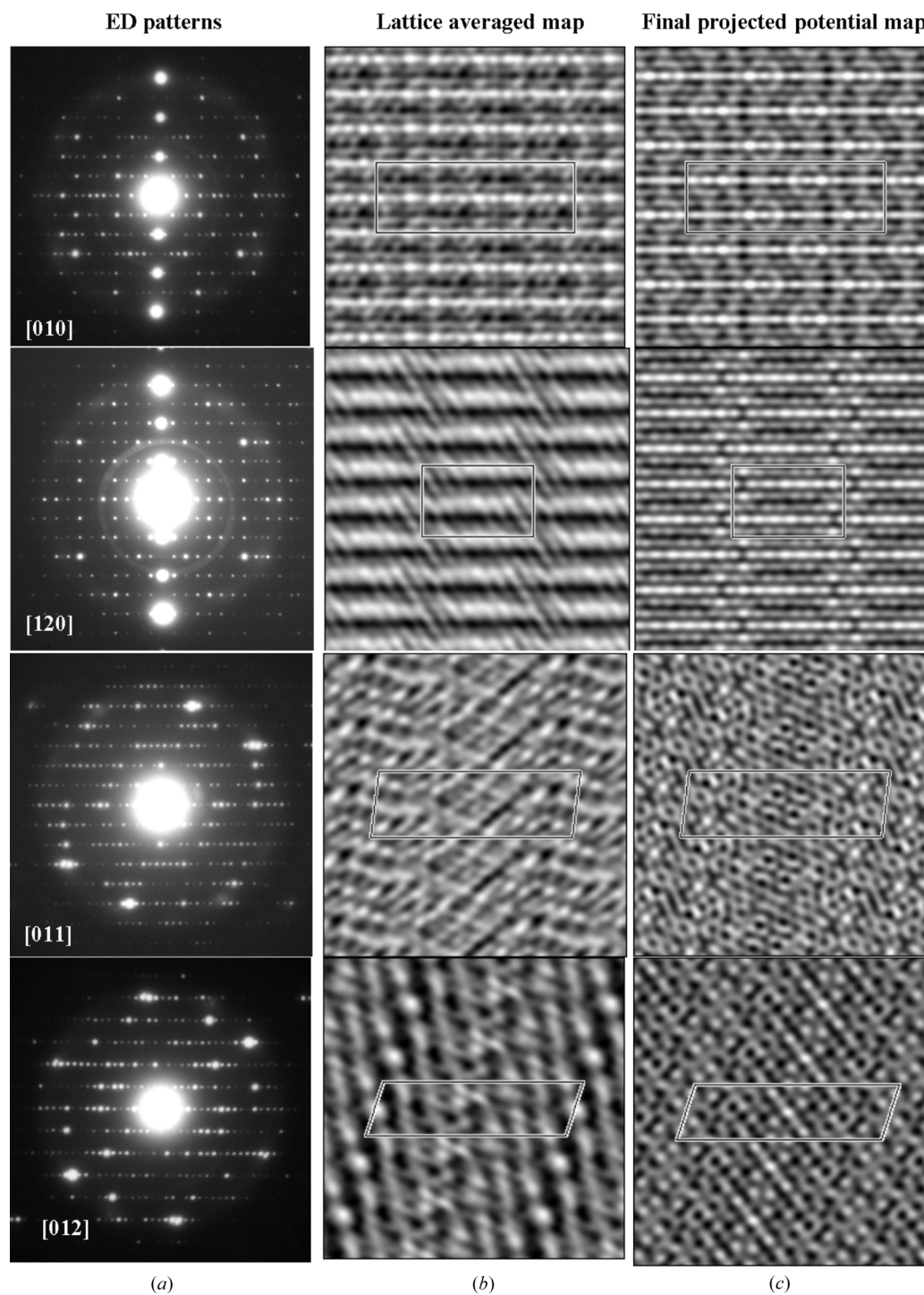


Figure 5

Image processing of four different zone axes [010], [120], [011] and [012]. Column (a): ED patterns of the corresponding zone axes. Column (b): lattice averaged maps of the original images. Column (c): the final projected potential maps using amplitudes from ED patterns and phases from images after CTF correction and imposing the symmetry.

but relative to an origin, the phase restriction and phase relations are only valid when the origin is on the specific symmetry element of the respective 2D symmetry, as given in *International Tables for Crystallography* (1983), Volume A. For each 2D symmetry, *CRISP* searches for the best origin at which the experimental phases deviate least from the ideal phase relations and phase restrictions. The average phase error (ϕ_{Res}) is calculated. The 2D symmetry of the projection can be determined by comparing the phase errors of different symmetries.

In the case of the [001] zone axis, the projection symmetry is $p6$. In $p6$, the origin should coincide with the sixfold axis. All phases should be 0 or 180° and the symmetry-related reflections should have the same phases:

$$\phi(hk0) = \phi(k, -h - k, 0) = \phi(h + k, -k, 0).$$

These phase restrictions and phase relations were imposed on the experimental phases by setting first the symmetry-related reflections equal and then to 0 or 180° , depending on which value they were closer to (Table 1). The amplitude-weighted phase residuals for the reflections within different resolution ranges indicated that the phases are reliable up to a resolution of about 1.95 Å. All reflections outside 1.95 Å resolution were weak and they were excluded in the final processing.

Although the amplitudes from the two images in Fig. 1 differ quite a lot, the phases agree extremely well; among the 110 strongest of the 220 reflections from both images, 84 of the 88 common reflections have the same phases. The 50 reflections with highest ED amplitudes are listed in Table 1.

The symmetry was also imposed on the amplitudes by averaging the amplitudes of the symmetry-related reflections. This step will eliminate most of the effects of crystal tilt.

4.5. Projected potential map

Different maps were calculated by inverse Fourier transformation of the amplitudes and phases of all reflections at different stages of image processing. Lattice averaged maps were obtained from the amplitudes and phases directly as extracted from the images, before the CTF correction and imposing the symmetry.

The lattice averaged maps from image 1 and image 2 are very different (Figs. 4*a* and *b*). One of the reasons is crystal tilt. When a crystal is tilted, black and white dots in the image/lattice averaged map are smeared out in the direction perpendicular to the tilt axis. Consequently, amplitudes especially of those reflections further away from the tilt axis in the Fourier transform are dampened (Zou, 1995). From both the images/lattice averaged maps and the Fourier transforms, it is obvious that image 1 suffers more crystal tilt than image 2 (Fig. 1 and Figs. 4*a*, *b*). However, phases are not affected by a slight crystal tilt, as can be seen from Table 1.

The effects of crystal tilt are largely compensated for by imposing the symmetry on the amplitudes and phases (Hovmöller & Zou, 1999). After imposing the $p6$ symmetry, both maps obtained from images 1 and 2 show well resolved

Table 2

Summary of the image processing of HREM images from all 13 zone axes.

Zone axis	2D symmetry	No. of unique reflections	Rsym	ϕ_{Res} ($^\circ$)
[001]	$p6$	216	27.9	25.3
[001]	$p6$	220	22.6	27.1
[010]	pmg	100	65.8	24.0
[120]	pmg	51	25.2	27.1
[5, 18, 0]	pmg	19	43.4	25.8
[011]	$p2$	224	–	25.5
[012]	$p2$	132	–	30.6
[013]	$p2$	201	–	21.5
[014]	$p2$	143	–	17.9
[021]	$p2$	129	–	28.5
[023]	$p2$	120	–	24.3
[121]	$p2$	137	–	19.8
[122]	$p2$	204	–	18.1
[241]	$p2$	52	–	20.8

dots (Figs. 4*c* and *d*). However, the map from image 1 (Fig. 4*c*) shows white dots while the map from image 2 shows black dots (Fig. 4*d*). This is because the images were taken at different defocus conditions. When the CTF is also compensated for, by adding 180° to the phases of those reflections that are at the negative CTF, the maps from image 1 (Fig. 4*e*) and image 2 (Fig. 4*f*) become very similar, and these are the final projected potential maps. Since white contrast corresponds to high projected potential in the crystal, white dots in the map correspond to atom rows in the projections. The white dots in Fig. 4(*e*) are better separated than those in Fig. 4(*f*), indicating that the resolution is somewhat higher in the map from image 1 than that from image 2. The great similarity of the projected potential maps reconstructed from HREM images of two different crystals taken at quite different conditions demonstrates the power of image processing. The amplitudes and especially the phases obtained from HREM images by crystallographic image processing are reliable.

Images taken along the other 12 zone axes were processed in a similar way and amplitudes and phases of the structure factors were extracted. The results of image processing are summarized in Table 2 and Fig. 5. Three zone axes, [010], [120] and [5, 18, 0] have pmg symmetry while the other nine zone axes have only $p2$ symmetry. The number of unique reflections from each zone axis varied between 19 and 224. The amplitude-weighted phase residuals for data up to 1.95 Å varied between 17.9 and 30.6° for different zone axes (Table 2).

Also, the amplitudes from HREM images are modulated by the CTF. It is difficult to compensate for these effects completely, especially near the cross overs of the CTF. Furthermore, for those projections with $p2$ symmetry, crystal tilt cannot be compensated for by imposing the symmetry, since reflections have only their Friedel pairs as symmetry-related reflections. For these reasons, we used amplitudes from the ED patterns (Fig. 5) instead of the amplitudes from the HREM images. The amplitudes were calculated as the square root of the intensities extracted from the corresponding ED patterns of an exposure series.

5. 3D reconstruction

Owing to the large unit cell of ν -AlCrFe, many atoms overlap in every projection. Images have to be combined to obtain a 3D potential map in order to resolve the individual atoms. Two important steps are needed for 3D reconstruction: converting the 2D indices into 3D indices and putting all images into a common origin.

Firstly, the 3D indices of two reflections in the Fourier transform of each image are determined from the 3D reciprocal space reconstructed from three tilt series of electron diffraction (Fig. 1). Then all reflections in the Fourier transform of the image are converted from the indices of these two reflections into 3D indices in *CRISP*. The corresponding symmetries are imposed on amplitudes and phases.

Since phases are related to the origin, we have to find a common origin for all the projections and shift the phases accordingly to the common origin. We choose the origin given for $P6_3/m$ by *International Tables for Crystallography* (1983), Volume A. The origin is on the 6_3 axis, halfway between the mirror planes. There are two such origins in each unit cell, at $z = 0$ and $z = 0.5$.

CRISP locates the origin of the projected unit cell at the origin of the corresponding 2D plane group defined by *International Tables for Crystallography* (1983), Volume A. In

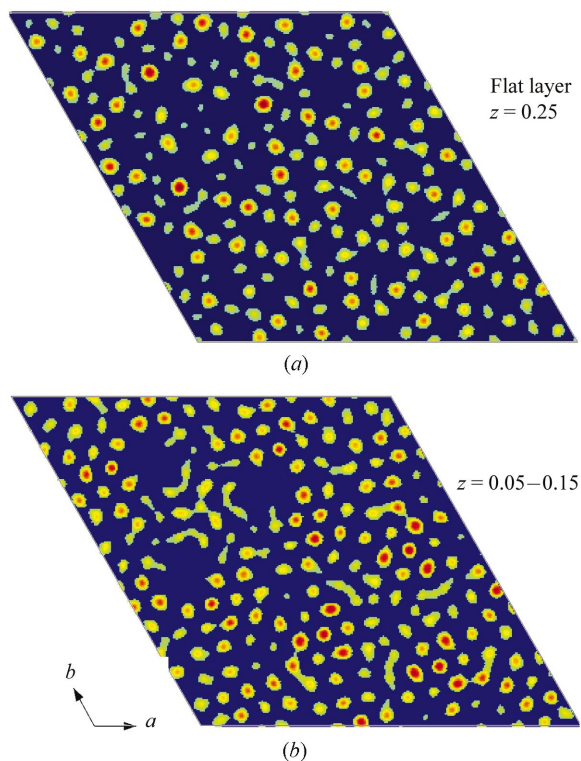


Figure 6 Sections of the 3D potential map obtained by electron crystallography; (a) the flat layer (*F*) at $z = 0.25$; (b) the puckered layer (*P*) at $z = 0.10 \pm 0.05$. In general, the strong peaks correspond to Fe/Cr atoms while the weak peaks are Al. 131 unique peaks were found, out of which 7 were removed due to too short interatomic distances. 124 unique atoms were assigned from these potential maps, out of which 115 atomic positions agree very closely (differ by less than 0.85 \AA) with those obtained by X-ray crystallography (Mo *et al.*, 2000).

most cases, the origin coincides with the highest symmetry element. For the projection along the $[001]$ zone axis, the origin is unique at the sixfold axis (6_3 axis in 3D). In projections along all other zone axes (having pmg and $p2$ symmetry), there are four mathematically equivalent origins per unit cell; at $(xy) = (00)$, $(\frac{1}{2}0)$, $(0\frac{1}{2})$ and $(\frac{1}{2}\frac{1}{2})$, respectively. The detailed procedures are the following:

(i) The origin in 3D is fixed from the $[001]$ and the $[010]$ projections. The origin in the ab plane was fixed to the 6_3 axis, which is at the sixfold axis of the $[001]$ projections. The origin along the c axis was set to the same origin determined from the $[010]$ projection. This leaves only two possibilities for the origin of the $[010]$ zone axis, at (00) or $(\frac{1}{2}0)$. The final origin is determined by considering the agreement of the phases of the common reflection row $h00$ ($h = 2n + 1$) with those already fixed in the $[001]$ projections (the $h00$ reflections with even h indices are seminvariants, *i.e.* their phases are fixed independently of the choice of origin, so they cannot be used for fixing the origin).

(ii) The origin for each of the other $[0vw]$ zone axes was determined in a similar way, by comparing the phases of those reflections that are common with the $[001]$ and $[010]$ zone axes.

(iii) The origin for each of the $[u,2u,w]$ projections was determined by comparing the phases of those reflections that

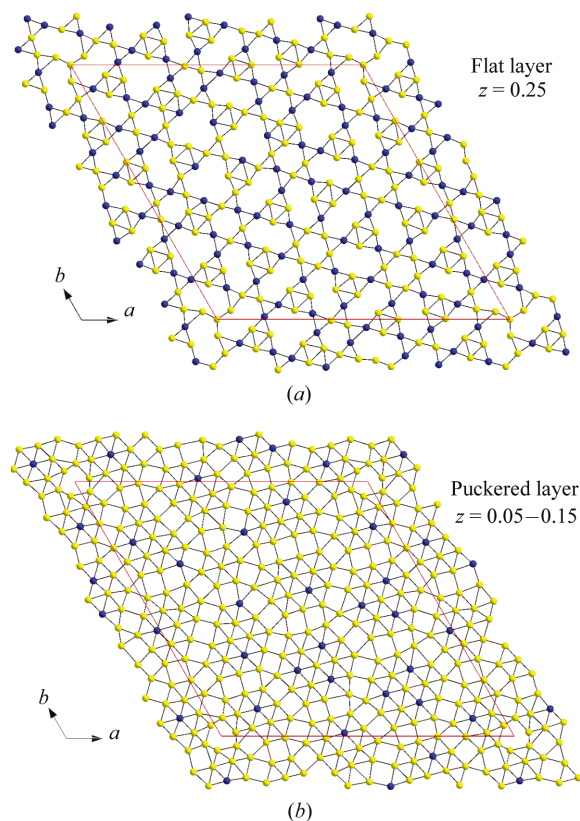


Figure 7 Structure model of the ν phase determined by electron crystallography. (a) The flat layer and (b) the puckered layer. Atoms that are less than 3.6 \AA from each other are connected. The transition atoms are in blue and Al atoms are in yellow.

are in common with the [001] and [0 νw] zone axes. For example, $-2h, h, 0$ reflections exist in both the [121] and [001] zones. We could shift the origin until most of the common reflections had the same phases.

When the origin has been found for a projection, the phases of all reflections in this projection are shifted from the 2D origin at (00), with phase $\phi_{\text{old}}(hk)$, onto the new common 3D origin at (xy). This results in a phase shift. The new phases [$\phi_{\text{new}}(hk)$] are calculated using

$$\phi_{\text{new}}(hk) = \phi_{\text{old}}(hk) + 360^\circ(hx + ky).$$

The ED intensities obtained from each zone axis were scaled together by the program *Triple* (Calidris, 2000b) using all common reflections. The merging procedure plays an important role in the final result, since intensities of the common reflections from different zone axes are different due to dynamic effects. Unfortunately, the [001] zone, which contains more reflections than any other zone, is the one suffering most from dynamical effects. Thus we waited to the end before merging these data. We first merged reflections of all the [0 νw] zone axes, using the common row of reflections $h00$. The R_{merge} values were all in the range 11–23%. Then reflections from all the [$u, 2u, w$] zone axes were merged, using the common row $2h, -h, 0$, in the order [120], [121], [122] and [241]. The R_{merge} values (%) were 17.3, 16.6 and 19.4,

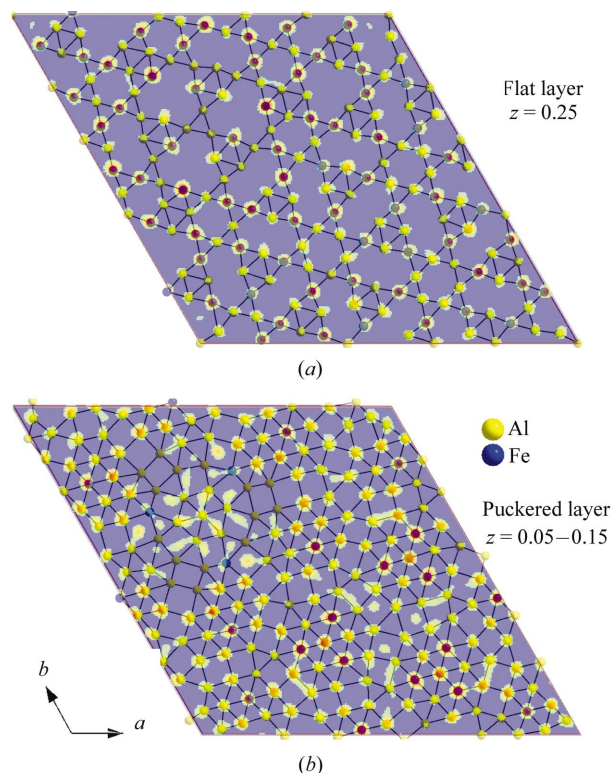


Figure 8

The structure model in Fig. 7 superimposed on the potential maps in Fig. 6. (a) Flat layer and (b) puckered layer. In the flat layer, only one unique peak near the origin does not correspond to atoms. In the puckered layer, one unique peak near one threefold axis at $(\frac{2}{3}, \frac{1}{3}, 0)$ and five unique peaks near the other threefold axis at $(\frac{1}{3}, \frac{2}{3}, 0)$ do not correspond to atoms. Five atoms are added around the threefold axis at $(\frac{1}{3}, \frac{2}{3}, 0)$ on the puckered layer and do not correspond to any peaks in (b).

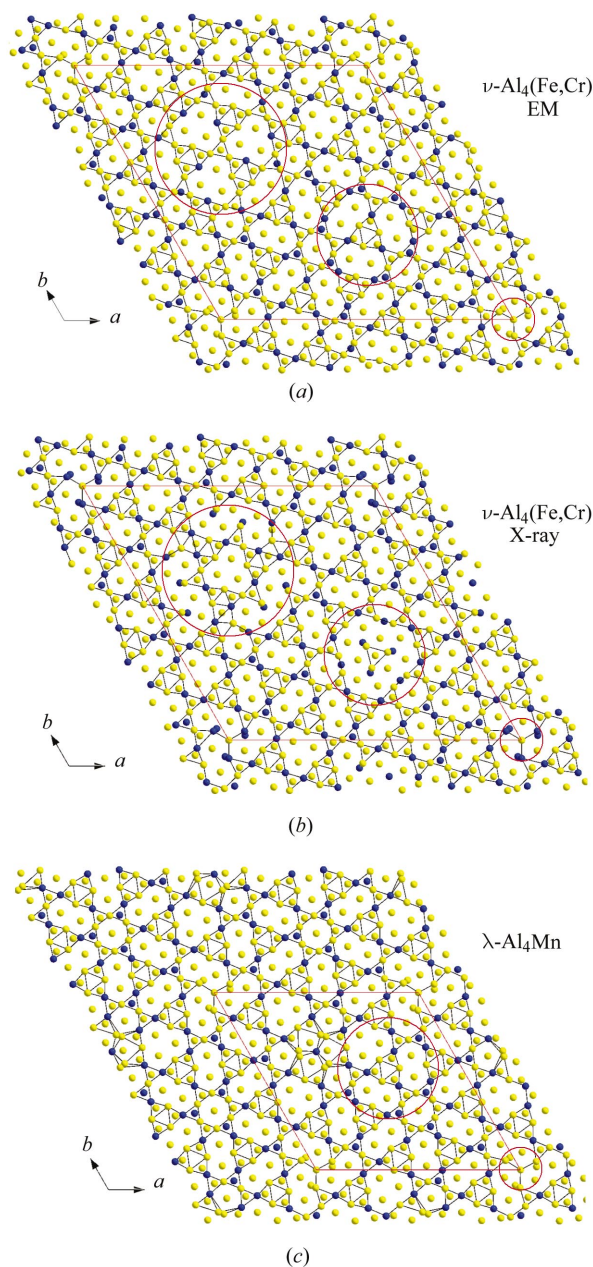


Figure 9

Structure models of the three layers FPF'' constituting half of the unit cell from (a) $\nu\text{-AlFeCr}$ obtained by electron crystallography, (b) $\nu\text{-AlFeCr}$ obtained by X-ray crystallography and (c) $\lambda\text{-Al}_4\text{Mn}$ obtained by X-ray crystallography. All the connected atoms are in the flat layers and the isolated atoms are in the puckered layers. The transition-metal atoms are in blue and Al in yellow. The six blue atoms around the origin in (b) are mixed Al/TM atoms with half occupancy each. All atoms except for some around the 6_3 axis and threefold axes (within the marked red circles) are located at very similar positions in (a) and (b). Also, the Al and TM assignments are the same. The main differences in the small circles for (a), (b) and (c) are the atoms on the 6_3 axis. One atom is found at $z = 0.25$ in (a), two atoms with half occupancy each are found in (b), at $z = 0.25$ and $z = 0.110$, respectively, and one atom with 74% occupancy is found at $z = 0.138$ in (c). Around one of the threefold axes of $\nu\text{-AlFeCr}$ (marked by the medium-sized circles), the atomic arrangements in (a) are slightly different from those in (b), but most of those in (a) are similar to those in (c), although there is no true threefold axis at this position in (c). The largest difference between (a) and (b) is within the large circles, for which there is no corresponding atomic arrangement in $\lambda\text{-Al}_4\text{Mn}$ owing to its smaller unit cell.

Table 3

The 150 strongest of the total 304 structure factors with amplitudes from ED patterns and phases from images that were used for 3D reconstruction.

<i>h</i>	<i>k</i>	<i>l</i>	Amp.	Phase	<i>h</i>	<i>k</i>	<i>l</i>	Amp.	Phase	<i>h</i>	<i>k</i>	<i>l</i>	Amp.	Phase
3	8	5	8643	180	14	1	1	1086	0	3	14	0	843	180
0	0	6	8627	180	5	14	0	1079	180	1	11	3	838	180
14	5	0	6452	0	12	1	3	1074	180	2	5	1	837	0
5	13	2	6321	180	2	9	0	1073	180	1	3	1	836	180
10	6	3	5917	180	12	6	0	1069	0	3	5	1	836	0
5	13	0	5247	0	13	4	0	1056	0	5	15	0	835	0
2	5	5	4371	0	11	6	3	1052	180	5	5	0	833	180
13	2	3	4342	0	0	6	1	1049	0	8	11	0	827	0
0	0	2	3238	180	5	1	5	1040	0	9	8	2	811	180
12	3	3	2630	180	15	1	0	1017	0	0	8	2	803	0
11	7	0	2256	0	7	10	0	1008	0	12	3	1	802	180
3	8	4	2192	0	4	2	5	984	180	12	5	0	799	0
14	4	0	2080	180	2	6	1	984	180	1	3	3	782	180
13	2	0	1943	180	0	6	5	969	0	2	2	3	774	0
12	5	3	1928	0	0	9	0	961	180	1	5	5	773	180
0	0	4	1856	0	9	8	3	958	0	5	7	4	769	180
10	6	0	1837	180	11	8	0	954	0	3	4	4	764	0
2	5	3	1787	180	5	4	2	934	0	13	3	1	759	0
9	8	0	1763	0	4	13	2	932	0	1	16	0	757	0
3	8	1	1737	180	14	3	0	931	0	7	2	5	756	0
10	6	2	1706	180	8	1	4	924	180	3	2	3	752	0
13	3	3	1618	0	6	4	4	920	180	3	4	2	751	0
3	5	5	1601	0	0	4	3	912	0	0	12	1	736	0
14	2	0	1593	180	10	6	4	912	0	4	2	1	733	0
6	4	2	1555	180	9	3	0	910	180	13	2	4	724	0
13	2	1	1503	0	5	9	3	907	0	13	6	0	724	0
3	7	5	1462	0	11	3	3	903	180	6	10	2	718	180
0	12	3	1427	0	2	5	4	903	0	8	7	2	710	180
2	8	5	1415	180	0	14	0	901	0	6	14	0	705	180
13	5	0	1372	180	10	7	3	900	0	15	2	0	702	180
3	8	0	1370	180	4	9	0	895	180	14	3	3	701	180
9	7	3	1349	180	1	14	0	892	180	1	4	6	701	0
17	4	0	1325	0	2	14	0	892	180	1	4	0	698	180
13	2	2	1313	180	2	5	6	889	180	2	10	4	691	180
8	1	2	1290	180	6	7	3	888	180	1	7	1	689	180
2	6	5	1267	180	6	10	0	888	0	9	9	0	684	0
2	4	5	1258	0	3	7	0	878	0	16	1	0	670	0
8	1	0	1243	180	7	13	0	878	180	12	4	0	668	0
11	5	3	1242	0	2	15	0	877	180	0	2	0	665	0
2	5	0	1241	0	0	14	2	875	0	0	4	0	663	180
15	7	0	1236	0	10	10	0	870	0	1	10	5	660	180
4	9	4	1235	180	12	7	0	866	0	4	11	0	655	0
14	1	0	1229	180	4	10	3	866	0	0	2	1	648	0
6	4	0	1211	180	4	8	0	862	180	3	12	2	647	0
9	3	2	1203	0	3	7	1	861	0	7	8	2	645	0
14	6	0	1160	0	6	12	2	860	180	9	6	2	642	180
3	9	4	1146	0	5	7	0	856	0	4	6	5	641	0
1	1	2	1123	0	15	4	0	854	180	6	12	0	638	0
2	8	1	1105	0	8	9	0	850	180	2	10	3	634	180
6	13	0	1102	0	12	1	2	847	180	0	1	2	632	0

respectively. Finally, these two data sets were merged with the [001] and [5, 18, 0] zone axis, in the order [001], [0 νw], [$u, 2u, w$] and [5, 18, 0]. The R_{merge} values (%) were 28.1, 26.6 and 24.4, respectively.

The phases derived from images were combined with the corresponding amplitudes from ED patterns and the data set of 3D structure factors was obtained. Since the phase residual increased abruptly beyond the 1.95 Å resolution, and weak reflections are readily distorted by dynamic scattering, noise and optical distortions and they do not contribute very much to the final map, only the 304 stron-

gest (of which 150 are listed in Table 3) out of 641 unique reflections to 1.95 Å resolution were used for further processing. The sum of the intensities of these strongest reflections accounted for 78% of the total intensities. A 3D potential map was calculated from the amplitudes and phases of the 304 strongest reflections by 3D inverse Fourier transformation, using the *3D-Map* software (Olynikov *et al.*, 2003). The sampling of the 3D map was chosen to be 0.1 Å pixel⁻¹ along the three main axes, sufficient to keep the 0.2 Å accuracy of atomic positions obtained from HREM with a resolution of 2 Å.

Table 4

Atomic coordinates determined by electron crystallography.

124 atoms were found by electron crystallography. Five atoms were added according to the geometry in the puckered layer and they are marked by *. 11 atoms differ by 1.2–1.7 Å from the X-ray model and they are marked by #. Atoms are numbered in such a way that they correspond to those determined by X-ray crystallography. Atoms 2, 16, 63, 101 and 102 of the X-ray model are not present in the table since there are no such corresponding atoms from EM. Atoms Al90b, Al96b and Al115b (marked by \$) are also close to the corresponding atoms in the X-ray model (differ by 1.2–1.5 Å), but they are in the flat layer instead of in the puckered layer in the X-ray model.

Atom	x	y	z	Atom	x	y	z	Atom	x	y	z
Al1	0.0000	0.0000	0.2500	Al46	0.6179	0.0000	0.2500	TM90#	0.4790	0.8020	0.0677
Al3#	0.3334	0.6667	0.0583	Al47	0.6526	0.1340	0.2500	Al90b\$	0.1861	0.6873	0.2500
TM4	0.0298	0.9057	0.2500	Al48	0.6725	0.2035	0.2500	Al91*#	0.4050	0.5850	0.0583
TM5	0.1787	0.8462	0.2500	Al49	0.7047	0.1216	0.2500	Al92	0.2084	0.8536	0.0583
TM6	0.3375	0.0224	0.2500	Al50	0.7121	0.3424	0.2500	Al93	0.2754	0.9727	0.1250
TM7	0.5534	0.3971	0.2500	Al51	0.7271	0.0298	0.2500	Al94	0.2953	0.9156	0.0667
TM8	0.7519	0.0968	0.2500	Al52	0.7420	0.2556	0.2500	Al95	0.3350	0.0496	0.0667
TM9	0.8437	0.2159	0.2500	Al53	0.7700	0.1700	0.2500	Al96*#	0.3150	0.8550	0.0667
TM10	0.9429	0.1811	0.2500	Al54	0.7817	0.0025	0.2500	Al96b\$	0.3499	0.8611	0.2500
TM11	0.9896	0.1563	0.2500	Al55	0.7916	0.2407	0.2500	Al97	0.3524	0.9901	0.0583
TM12	0.0397	0.7494	0.2500	Al56	0.8089	0.0868	0.2500	Al98#	0.3474	0.6377	0.2500
TM13	0.0670	0.6601	0.2500	Al57	0.8834	0.3474	0.2500	Al99	0.3697	0.9330	0.1333
TM14	0.1266	0.8710	0.2500	Al58	0.8859	0.1911	0.2500	Al100	0.4069	0.0669	0.1333
TM15	0.1439	0.7146	0.2500	Al59	0.9057	0.0397	0.2500	Al103	0.4467	0.9529	0.0500
TM17	0.2779	0.8114	0.2500	Al60	0.9082	0.2730	0.2500	Al104	0.4690	0.9057	0.1417
TM18	0.3151	0.9479	0.2500	Al61	0.9206	0.1067	0.2500	Al105	0.4839	0.0869	0.0583
TM19	0.3747	0.7742	0.2500	Al62	0.9652	0.2481	0.2500	Al106*#	0.4950	0.7520	0.1417
TM20	0.4591	0.0522	0.2500	Al64	0.7022	0.2382	0.0583	Al107	0.5012	0.0297	0.1417
TM21	0.4938	0.9677	0.2500	Al65#	0.7450	0.3550	0.5583	Al108	0.5236	0.9801	0.0667
TM22	0.6278	0.0620	0.2500	TM66	0.7419	0.1315	0.0667	Al109	0.5633	0.1390	0.0667
TM23	0.8114	0.3077	0.2500	TM67	0.0794	0.7618	0.0667	Al110	0.5906	0.0918	0.1417
TM24	0.8512	0.0596	0.2500	Al68	0.3871	0.8859	0.0500	Al111	0.6055	0.0323	0.0583
Al25	0.9653	0.0298	0.2500	TM69	0.4268	0.0124	0.0667	Al112	0.6228	0.2208	0.1417
Al26	0.0521	0.5930	0.2500	TM70	0.8933	0.0695	0.0583	TM113	0.6452	0.1663	0.0667
Al27	0.0744	0.8833	0.2500	Al71	0.9851	0.0422	0.0583	Al114	0.6675	0.1067	0.0583
Al28	0.0918	0.7345	0.2500	Al72	0.0025	0.8362	0.1333	Al115	0.6824	0.2953	0.0667
Al29	0.0993	0.9603	0.2500	Al73	0.0074	0.2208	0.1333	TM115b\$	0.6898	0.2779	0.2500
Al30	0.1092	0.8015	0.2500	Al74	0.0025	0.7395	0.0583	Al116	0.6849	0.0521	0.1333
Al31	0.1514	0.9405	0.2500	Al75	0.0249	0.1663	0.0583	Al117	0.7221	0.1861	0.1333
Al32	0.2060	0.7618	0.2500	Al76	0.0223	0.6848	0.1333	Al118	0.7618	0.0720	0.0583
Al33	0.2283	0.8288	0.2500	Al77	0.0323	0.9603	0.1500	Al119	0.7618	0.3201	0.1333
Al34	0.2457	0.9033	0.2500	Al78	0.0422	0.6328	0.0667	TM120	0.7766	0.2630	0.0667
Al35	0.3077	0.8859	0.2500	Al79	0.0571	0.9157	0.0583	Al121	0.7991	0.2060	0.0583
Al36#	0.3102	0.7196	0.1417	Al80	0.0620	0.8163	0.1333	Al122	0.8164	0.1489	0.1333
Al37	0.3871	0.9950	0.2500	Al81	0.0993	0.7072	0.0583	Al123	0.8163	0.0496	0.0500
TM38	0.4094	0.9082	0.2500	Al82	0.1166	0.6501	0.1250	Al124	0.8362	0.3548	0.0667
Al39	0.4367	0.7568	0.2500	Al83	0.1191	0.8933	0.0667	Al125	0.8561	0.2804	0.1333
Al40	0.4342	0.9776	0.2500	Al84	0.1365	0.8363	0.0583	Al126	0.8735	0.1266	0.1333
Al41	0.4615	0.8387	0.2500	Al85	0.1563	0.7816	0.1333	Al127	0.8734	0.2258	0.0667
Al42*#	0.4700	0.6650	0.1417	Al86#	0.1563	0.5608	0.2500	Al128	0.9131	0.0124	0.0583
Al43	0.5285	0.0967	0.2500	Al87*#	0.2050	0.4400	0.0667	Al129	0.9305	0.2010	0.0667
Al44	0.5459	0.1687	0.2500	Al88	0.1737	0.7295	0.0583	Al130	0.9454	0.1414	0.0583
Al45	0.5633	0.0248	0.2500	Al89	0.1935	0.9106	0.1417	Al131	0.9677	0.0893	0.1333

6. Structure model of the ν phase obtained by 3D reconstruction

The 3D potential map was examined section by section perpendicular to the c axis. There are six layers stacked along the c axis in each unit cell. Only two of these six layers are unique, one flat layer occurring twice (at $z = 0.25$ and 0.75) and one puckered layer occurring four times (at $z \approx 0.10, 0.40, 0.60$ and 0.90). Sections corresponding to the flat (F) and puckered (P) layers are shown in Figs. 6(a) and (b), respectively. The flat layers coincide with mirror planes. The stacking sequence is $PFPP^m(PFP^m)'$, where P^m relates to P via a mirror reflection on the flat layer, and the $(PFP^m)'$ block is related to the $PFPP^m$ block by a 6_3 operation along the c axis.

The potential maps were remarkably clear (Figs. 6a and b) with most of the peaks perfectly round and well resolved. 63 and 68 peaks were found from the density maps in the flat (Fig. 6a) and puckered layers (Fig. 6b), respectively. Out of the 131 peaks, one on the flat layer and six on the puckered layer were removed owing to too short atomic distances. The 31 strongest peaks (peaks 1–31), except for those at $z \sim 0.1333$ (four peaks) and one peak at $z = 0.25$ (Al57), were assigned to be transition-metal (TM) atoms (Fe or Cr). This is because no TM atoms are located at $z \sim 0.1333$ in other related compounds such as the κ -AlNiCr (Sato *et al.*, 1997; Marsh, 1998) and λ -Al₄Mn (Kreiner & Franzen, 1997) phases. Peaks 39 and 40 (TM20 and 24, respectively) were also assigned to be TM, since all other atoms with similar geometry are TM atoms. All

other peaks were assigned to be Al. However, a few of them could possibly be TM or shared between Al and TM.

In the flat layer, 62 atoms were found. The structure model of the flat layer obtained from the potential map (Fig. 6*a*) is shown in Fig. 7(*a*). The close agreement with the potential map can be judged from Fig. 8(*a*), where the model is superimposed on the potential map. Atoms on the puckered layer also formed reasonable distances with each other, except for those around one of the threefold axes, which has empty areas without any peaks (Fig. 6*b*). It was obvious that some atoms were missing there since all intermetallic alloys tend to be closely packed. Five missing atoms were added in the puckered layer based on the relative positions of the atoms in the flat layer. Three were at $z \sim 0.067$ and two at $z \sim 0.133$. The structure model of the puckered layer is shown in Fig. 7(*b*) and superimposed on the potential map (Fig. 6*b*) in Fig. 8(*b*). The final model has in total 129 crystallographically unique atoms. Their atomic coordinates are listed in Table 4. Most of the interatomic distances are around 2.4 Å, with only four between 2.0 and 2.2 Å.

Compared with the X-ray model, 110 atoms differ by less than 0.31 Å (mean error 0.14 Å), 90 of those atoms differ by less than 0.20 Å (mean error 0.12 Å). Five atoms differ by 0.31–0.85 Å (mean error 0.59 Å). There are 14 atoms that differ from the X-ray model by more than 1.2 Å, and those are all around the three threefold axes (Figs. 9*a* and *b*).

7. Discussion

Our results show that it is possible to solve extremely complicated inorganic structures, with over 100 unique atoms, by electron crystallography. The fact that nearly all inorganic crystal structures that were solved by electron crystallography until now had one very short unit-cell dimension (typically about 4 Å) may have given the impression that the method is limited to such structures, where all atoms can be resolved in a single projection. The shortest unit-cell dimension of ν -AlFeCr is 12.5 Å and six different layers of atoms overlap when projected along that axis. Needless to say, any other projection (axial or not) will result in even more overlapping atoms.

Thus, it is not possible to solve a structure of this complexity from single projections, even if sub-ångström resolution electron microscopes are used. However, in three dimensions all atoms in intermetallic compounds are already well resolved in a 2 Å map, since the interatomic distances are around 2 Å. Provided sufficiently many of the most important reflections out to about 2.0 Å resolution are included in the 3D reconstruction (with correct phases), virtually all metal atoms will be seen in the first density map.

It should be stressed that, at this step of a structure determination, the crystallographic structure-factor phases are much more important than the amplitudes. If just a single very strong reflection is included with wrong phase, the density map is typically uninterpretable.

For a more general structure, the message is that the amplitudes of all unique reflections must be estimated, for

example from ED patterns, in order to be sure that the 3D map includes all the strongest reflections. At this stage, the amplitudes do not need to be very accurately measured, but all the phases should be correct. For most structures, it will be necessary to have about one to five reflections per unknown atom or just the strongest 10% of all reflections. This is similar to the data used for generating triplet relations in direct methods in X-ray crystallography where also only 10% of all reflections are used, namely those with the highest E values.

A complete structure determination contains the two distinct steps: solving and refining the structure. The refinement can only be started after the structure has been solved. By solving a structure, we mean that most of the most strongly scattering atoms are found to within an accuracy of 0.2 to 0.3 Å. All methods for solving crystal structures from X-ray diffraction data in most cases give just a fraction of the complete structure. Patterson methods give only the heaviest metals; direct methods do not give H atoms for organic structures *etc.* This is no problem since the remaining atoms are readily seen in difference Fourier maps, once these initial atoms are positioned. In the case of ν -AlFeCr, over 96% of all atoms were clearly resolved in the 3D map calculated from only a limited amount of all reflection data to 2.0 Å resolution. It is quite remarkable that this map shows both the lighter and heavier atoms and that even the atomic type Al or Fe/Cr in most cases is evident from the peak heights.

The structure model we derived by electron crystallography is remarkably similar to the X-ray structure (Mo *et al.*, 2000). At least 115 unique atoms agree in the two structure determinations. There are only a few areas of different appearances in the maps obtained from these independent investigations. These are all in the vicinity of the 6_3 axis and the threefold axes, as marked in Figs. 9(*a*) and (*b*). Near the 6_3 axis (marked by small circle), the main differences are the atoms on the 6_3 axis. In the model obtained by electron crystallography (Fig. 9*a*), there is only one atom at $z = 0.25$ (flat layer). In the X-ray model (Fig. 9*b*), there are two atoms at $z = 0.25$ and $z = 0.110$, respectively, both with half occupancy. In the λ -Al₄Mn (Fig. 9*c*), only one atom was found, at $z = 0.138$ with 74% occupancy. Around one threefold axis in ν -AlFeCr (marked by a medium-sized circle), the model obtained by electron crystallography (Fig. 9*a*) is quite similar to that of the λ -Al₄Mn (Fig. 9*c*), although there is no true threefold axis in λ -Al₄Mn. Atoms around the other threefold axis (marked by a large circle in Figs. 9*a* and *b*) are more uncertain, since all five atoms that were not directly found from the 3D potential map but added in the puckered layer based on the relative positions of the atoms in the flat layer, are located here. These last uncertain atoms remain to be verified by a careful structure refinement. For a structure refinement, as many reflections as possible should be included. The phases are not needed at the refinement stage, but if possible complete 3D data out to 1 Å resolution should be used. Strong and weak reflections are equally important. Such data can be obtained by electron diffraction, which is not affected by the contrast transfer function of the electron microscope, but suffers from dynamical scattering. The higher the accuracy of the amplitudes,

the more accurate will the atomic positions become. For smaller structures than ν -AlFeCr, it has been possible to reach accuracies of 0.01 to 0.02 Å (Weirich *et al.*, 1996, 2000). Such refinement is now in progress for ν -AlFeCr.

8. Conclusions

3D reconstruction from HREM images offers a new possibility for *ab initio* structure determination of inorganic compounds existing only with very small crystal sizes. 3D reconstruction can be applied to structures too complex to be solved by direct methods even using single-crystal X-ray diffraction, using a moderately high voltage electron microscope. There is no limit in terms of the number of unique atoms in a structure that can be solved by 3D reconstruction.

Peter Olynikov is thanked for writing the software *3D-Map*. This study was supported by grants from the Swedish Research Council (VR) and the National Natural Science Foundation of China, and from the European Commission to the project New Frontiers in Structural Biology. XDZ is a research fellow of the Royal Swedish Academy of Sciences supported by a grant from the Knut and Alice Wallenberg Foundation.

References

- Calidris (2000a). Manual for the Kite CCD camera. Manhemsvägen 4, SE-106 91, Sollentuna, Sweden.
- Calidris (2000b). *Triple* manual. Manhemsvägen 4, SE-106 91, Sollentuna, Sweden.
- Gemmi, M., Righi, L., Calestani, G., Migliori, A., Speghini, A., Santarosa, M. & Bettinelli, M. (2000). *Ultramicroscopy*, **84**, 133–142.
- Gjønnnes, J., Hansen, V., Berg, B. S., Runde, P., Cheng, Y. F., Gjønnnes, K., Dorset, D. L. & Gilmore, C. J. (1998). *Acta Cryst.* **A54**, 306–319.
- Hovmöller, S. (1992). *Ultramicroscopy*, **41**, 121–135.
- Hovmöller, S., Sjögren, A., Farrants, G., Sundberg, M. & Marinder, B.-O. (1984). *Nature (London)*, **311**, 238–241.
- Hovmöller, S. & Zou, X.D. (1999). *Microsc. Res. Techn.* **46**, 147–159.
- International Tables for Crystallography* (1983). Vol. A, edited by Th. Hahn. Dordrecht: Reidel. Present distributor Kluwer Academic Publishers.
- Kreiner, G. & Franzen, H. F. (1997). *J. Alloys Compds.* **261**, 83–104.
- Li, X. Z., Hiraga, K. & Yamamoto, A. (1997). *Philos. Mag.* **A76**, 657–666.
- Marsh, R. E. (1998). *Acta Cryst.* **B54**, 925–926.
- Mo, Z. M., Zhou, H. Y. & Kuo, K. H. (2000). *Acta Cryst.* **B56**, 392–401.
- Olynikov, O., Hovmöller, S. & Zou, X. D. (2003). *3D-Map*, a program for generating 3D Fourier map and determining peak positions. Structural Chemistry, Stockholm University, SE-106 91 Stockholm, Sweden.
- Sato, A., Yamamoto, A., Li, X. Z., Hiraga, K., Haibach, T. & Steurer, W. (1997). *Acta Cryst.* **C53**, 1531–1533.
- Wagner, P., Terasaki, O., Ritsch, S., Nery, J. G., Zones, S. I., Davis, M. E. & Hiraga, K. (1999). *J. Phys. Chem.* **B103**, 8245–8250.
- Wang, D. N., Hovmöller, S., Kihlberg, L. & Sundberg, M. (1988). *Ultramicroscopy*, **25**, 303–316.
- Wenk, H.-R., Downing, K. H., Hu, M. S. & O'Keefe, M. A. (1992). *Acta Cryst.* **A48**, 700–716.
- Weirich, T. E. (2001). *Acta Cryst.* **A57**, 183–191.
- Weirich, T. E., Ramlau, R., Simon, A., Hovmöller, S. & Zou, X. D. (1996). *Nature (London)*, **382**, 144–146.
- Weirich, T. E., Zou, X. D., Ramlau, R., Simon, A., Cascarano, G. L., Giacomozzo, C. & Hovmöller, S. (2000). *Acta Cryst.* **A56**, 29–35.
- Zandbergen, H. W., Andersen, S. J. & Jansen, J. (1997). *Science*, **277**, 1221–1225.
- Zou, X. D. (1995). *Electron Crystallography of Inorganic Structures – Theory and Practice. Chem. Commun.*, Vol. 5.
- Zou, X. D., Sukharev, Yu. & Hovmöller, S. (1993). *Ultramicroscopy*, **49**, 147–158.
- Zou, X. D., Sundberg, M., Larine, M. & Hovmöller, S. (1996). *Ultramicroscopy*, **62**, 103–121.